

# The surface diffuseness and the spin-orbital splitting in relativistic continuum Hartree-Bogoliubov theory

J. Meng and I.Tanihata<sup>a</sup>

*\*Department of Technical Physics, Peking University,  
Beijing 100871, P.R. China*

*<sup>a</sup>The Institute of Physical and Chemical Research (RIKEN)*

*Hirosawa 2-1, Wako-shi, Saitama, 351-0198 JAPAN*

*<sup>b</sup>Institute of Modern Physics, Chinese Academy of Sciences  
Lanzhou 730000, China*

*e-mail: meng@rikaxp.riken.go.jp*

February 6, 2008

## Abstract

The Relativistic Continuum Hartree Bogoliubov theory ( RCHB ), which is the extension of the Relativistic Mean Field and the Bogoliubov transformation in the coordinate representation, has been used to study tin isotopes. The pairing correlation is taken into account by a density-dependent force of zero range. RCHB is used to describe the even-even tin isotopes all the way from the proton drip line to the neutron drip line. The contribution of the continuum which is important for nuclei near the drip-line has been taken into account. The theoretical  $S_{2n}$  as well as the neutron, proton, and matter *rms* radii are presented and compared with the experimental values where they exist. The change of the potential surface with the neutron number has been investigated. The diffuseness of the potentials in tin isotopes is analyzed through the spin-orbital splitting in order to provide new way to understand the halo phenomena in exotic nuclei. The systematic of the isospin and

energy dependence of these results are extracted and analyzed.

PACS numbers : 21.10.Pc, 21.10.Gw, 21.60.-n, 21.60..Jz

Keywords: Relativistic continuum Hartree-Bogoliubov theory, spin-orbital splitting, zero range pairing force, potential diffuseness, canonical basis, tin isotopes

## 1. Introduction

Highly unstable nuclei with extreme proton and neutron ratio are now accessible with the help of the radioactive nuclear beam facilities. The extreme proton and neutron ratio of these nuclei and physics connected with these unprecedented low density matter have attracted worldwide attention in nuclear physics as well as other fields such as astrophysics. The recent research in this topic includes the detailed structure, its mode of excitation, and the reaction mechanism. Using the measured interaction cross sections it is possible to extract the nuclear root mean-square (*rms*) matter radii, the nuclear mass density and the other related observations. In these investigations, the observed sudden rise in the measured interaction cross-sections in the neutron rich light nuclei has been attributed to the corresponding large increase in the nuclear *rms* matter radii. This fact is an indication of the sudden change in the structure of these nuclei due to the addition of the last few neutrons. The celebrated example in these investigations is the discovery of the phenomenon of "neutron halo"<sup>1</sup>, for example in <sup>11</sup>Li. The neutron halo is a state in which neutrons spread like a thin mist around the nucleus. It is qualitatively associated with the very small separation energy ( $S_n$ ) of the last one or two neutrons. Due to this small value of  $S_n$  in such nuclei, the tail of its last neutron wavefunction and so also the corresponding density spreads far out from the center of the nucleus.

New theoretical models and techniques are being developed in order to describe unique phenomena in exotic nuclei far from the line of stability. Particularly, on the neutron-rich side, the property of exotic nuclei involves the weak binding of the outermost neutrons, the

coupling of bound state and the continuum, the diffuse particle distribution and isospin dependence of the shell structure. Due to their relevance to the r-process in nucleosynthesis, nuclei near the drip-line are also very important in nuclear astrophysics. As for the theoretical microscopic description of unstable nuclei is concerned, so far rather different techniques have been used, e.g., the Relativistic Continuum Hartree-Bogoliubov ( RCHB ) theory<sup>2-4</sup>; the exact solution of few-body equations treating inert sub-clusters as point particles<sup>5</sup>; the Skyrme Hartree-Fock-Bogoliubov ( HFB ) theory<sup>6,7</sup>; and two-frequency shell model<sup>8</sup>.

The few body method and a shell model diagonalization start by fitting the ground state properties of the nuclei or neighboring nuclei and aim at predicting the excited state properties. Whereas the relativistic and conventional mean field approaches are based on the description of global experimental data for nuclei throughout the nuclear chart. The principal goal here is to obtain a fair description of bulk properties, particularly for the ground states. The mean field has certain advantages in describing and predicting quantities, such as the radii, mass, tunneling probabilities, etc., in stable nuclei and their future extendability to exotic nuclei when the continuum is properly taken into account.

The RCHB theory, which is the extension of the Relativistic Mean Field ( RMF ) and the Bogoliubov transformation in the coordinate representation, provides not only a unified description of mean field and pairing correlation but also the proper description for the continuum and the coupling between the bound state and the continuum<sup>4</sup>.

Recently, a fully self-consistent description of the chain of Lithium isotopes ranging from  ${}^6\text{Li}$  to  ${}^{11}\text{Li}$  has been given by the RCHB<sup>2</sup>. The halo in  ${}^{11}\text{Li}$  has been successfully reproduced in this self-consistent picture. Excellent agreement with recent experimental data on the radii, binding energy and density distribution is obtained. This remarkable success is mainly attributed to the proper treatment of the continuum states and the pairing by solving the RCHB equations. This procedure helps to incorporate correctly the scattering of Cooper pairs to the  $2s_{1/2}$  level, which is more close to the threshold than the  $1d_{5/2}$  and  $1d_{3/2}$  levels, in the continuum. The contribution from the continuum is proved to be crucial. Therefore

the relativistic mean field provides another picture of halo in nuclei: Due to the extreme low proton to neutron ratio, the surface of the neutron potentials become highly diffuse. Because the orbital with small orbital angular momentum has less centrifugal barrier, the particles with weak binding or even in the continuum in these orbital will have more chance to tunnel. In order to study the influence of correlation and many-body effects, it would be very interesting to find also nuclei with a larger number of neutron distributed in the halo. Based on the RCHB, a new phenomenon "Giant Halo" has been predicted in the Zr nuclei close to the neutron drip line, which are composed not only by one or two neutrons, as is the case in the halos investigated so far in light *p*-shell nuclei, but which contain up to 6 neutrons<sup>3</sup>.

The development of a proton skin as well as neutron skin in Na isotopes has been systematically studied with RCHB in Ref.<sup>9</sup>, where the pairing and blocking effect have been treated self-consistently. A Glauber model calculation has been carried out with the density obtained from RCHB. A good agreement has been obtained with the measured cross sections for <sup>12</sup>C as a target and a rapid increase of the cross sections has been predicted for neutron rich Na isotopes beyond <sup>32</sup>Na. After systematic examination of the neutron, proton and matter distributions in the Na nuclei from the proton drip-line to the neutron drip-line, a relation between the tail part of the density and the shell structure has been found. The tail of the matter distribution is not so sensitive to how many particles are filled in a major shell. Instead it is very sensitive to whether this shell has been occupied or not. The physics behind the skin and halo has been revealed as a spatial demonstration of shell effect: simply the extra neutrons are filled in the next shell and sub-shell. This is in agreement with the mechanism observed so far in the halo system but more general.

From the mean field point of view, the properties of all the nucleons in the nuclei are determined by the mean potential provided by their interaction with the other nucleons. Therefore the study of the isospin dependence of the potential, which become highly diffuse near the particle drip line, is crucial to understand unstable nuclei and the study of the

surface diffuseness will provide another mean to understand exotic nuclei. In the present work, we extend our former investigation and study the surface diffuseness, the isospin dependence of the potential, and spin-orbital splitting in tin isotopes. For exotic nuclei, as orbitals with small orbital angular momentum near the threshold will extend far out from the nuclear center, and thus the pairing correlation can couple the bound states and positive energy states. Particularly on the neutron-rich side, as neutron carries no electric charge, the neutron drip line is located very far from the valley of  $\beta$ -stability. It is crucial to understand how the isospin dependence of the potential and the diffuseness develops in unstable nuclei. The surface diffuseness can be strongly related with the spin-orbital splitting, which could be measured experimentally.

In the present study, isospin dependence of the potential diffuseness, their relation with the spin-orbital splitting, and the ground-state properties of drip-line systems are investigated by means of the self-consistent RCHB approach. The shell structure and its isospin dependence in tin isotope is discussed in the canonical basis. The isospin-dependence and energy-dependence of the neutron spin-orbit splitting are discussed. An outline of the RCHB formalism is briefly reviewed in Sec. II. In Sec. III, the isospin-dependence and energy-dependence of the neutron spin-orbit splitting, the neutron, proton, and matter density distributions are presented for Sn isotopes. A brief summary is given in the last section.

## 2. RCHB Theory

The RCHB theory, which is the extension of the RMF and the Bogoliubov transformation in the coordinate representation, is suggested in Ref.<sup>2</sup>, its detailed formalism and numerical solution can be found in Ref.<sup>4</sup> and the references therein. The basic ansatz of the RMF theory is a Lagrangian density whereby nucleons are described as Dirac particles which interact via the exchange of various mesons and the photon. The mesons considered are the scalar sigma ( $\sigma$ ), vector omega ( $\omega$ ) and iso-vector vector rho ( $\vec{\rho}$ ). The rho ( $\vec{\rho}$ ) meson provides the necessary isospin asymmetry. The scalar sigma meson moves in a self-interacting field

having cubic and quadratic terms with strengths  $g_2$  and  $g_3$  respectively. The Lagrangian then consists of the free baryon and meson parts and the interaction part with minimal coupling, together with the nucleon mass  $M$ , and  $m_\sigma$ ,  $g_\sigma$ ,  $m_\omega$ ,  $g_\omega$ ,  $m_\rho$ ,  $g_\rho$  the masses and coupling constants of the respective mesons and:

$$\begin{aligned} \mathcal{L} = & \bar{\psi}(i\cancel{\partial} - M)\psi + \frac{1}{2}\partial_\mu\sigma\partial^\mu\sigma - U(\sigma) - \frac{1}{4}\Omega_{\mu\nu}\Omega^{\mu\nu} \\ & + \frac{1}{2}m_\omega^2\omega_\mu\omega^\mu - \frac{1}{4}\vec{R}_{\mu\nu}\vec{R}^{\mu\nu} + \frac{1}{2}m_\rho^2\vec{\rho}_\mu\vec{\rho}^\mu - \frac{1}{4}F_{\mu\nu}F^{\mu\nu} \\ & - g_\sigma\bar{\psi}\sigma\psi - g_\omega\bar{\psi}\psi\psi - g_\rho\bar{\psi}\vec{\rho}\vec{\tau}\psi - e\bar{\psi}\vec{A}\psi. \end{aligned} \quad (1)$$

The field tensors for the vector mesons are given as:

$$\begin{cases} \Omega^{\mu\nu} = \partial^\mu\omega^\nu - \partial^\nu\omega^\mu, \\ \vec{R}^{\mu\nu} = \partial^\mu\vec{\rho}^\nu - \partial^\nu\vec{\rho}^\mu - g^\rho(\vec{\rho}^\mu \times \vec{\rho}^\nu), \\ F^{\mu\nu} = \partial^\mu\vec{A}^\nu - \partial^\nu\vec{A}^\mu. \end{cases} \quad (2)$$

For a realistic description of nuclear properties a nonlinear self-coupling for the scalar mesons turns crucial<sup>10</sup>:

$$U(\sigma) = \frac{1}{2}m_\sigma^2\sigma^2 + \frac{g_2}{3}\sigma^3 + \frac{g_3}{4}\sigma^4 \quad (3)$$

The classical variation principle gives the following equations of motion :

$$[\vec{\alpha} \cdot \vec{p} + V_V(\vec{r}) + \beta(M + V_S(\vec{r}))]\psi_i = \epsilon_i\psi_i \quad (4)$$

for the nucleon spinors and

$$\begin{cases} (-\Delta\sigma + U'(\sigma)) = g_\sigma\rho_s \\ (-\Delta + m_\omega^2)\omega^\mu = g_\omega j^\mu(\vec{r}) \\ (-\Delta + m_\rho^2)\vec{\rho}^\mu = g_\rho\vec{j}^\mu(\vec{r}) \\ -\Delta A_0^\mu(\vec{r}) = ej_\rho^\mu(\vec{r}) \end{cases} \quad (5)$$

for the mesons, where

$$\begin{cases} V_V(\vec{r}) = g_\omega\psi + g_\rho\vec{\rho}\vec{\tau} + \frac{1}{2}e(1 - \tau_3)\vec{A}, \\ V_S(\vec{r}) = g_\sigma\sigma(\vec{r}) \end{cases} \quad (6)$$

are the vector and scalar potentials respectively and the source terms for the mesons are

$$\begin{cases} \rho_s &= \sum_{i=1}^A \bar{\psi}_i \psi_i \\ j^\mu(\vec{r}) &= \sum_{i=1}^A \bar{\psi}_i \gamma^\mu \psi_i \\ \vec{j}^\mu(\vec{r}) &= \sum_{i=1}^A \bar{\psi}_i \gamma^\mu \vec{\tau} \psi_i \\ j_p^\mu(\vec{r}) &= \sum_{i=1}^A \bar{\psi}_i \gamma^\mu \frac{1 - \tau_3}{2} \psi_i, \end{cases} \quad (7)$$

where the summations are over the valence nucleons only. It should be noted that as usual, the present approach neglects the contribution of negative energy states, i.e., no-sea approximation, which means that the vacuum is not polarized. The coupled equations Eq.(4) and Eq.(5) are nonlinear quantum field equations, and their exact solutions are very complicated. Thus the mean field approximation is generally used: i.e., the meson field operators in Eq.(4) are replaced by their expectation values. Then the nucleons move independently in the classical meson fields. The coupled equations are self-consistently solved by iteration.

For spherical nuclei, i.e., the systems with rotational symmetry, the potential of the nucleon and the sources of meson fields depend only on the radial coordinate  $r$ . The spinor is characterized by the angular momentum quantum numbers  $l, j, m$ , the isospin  $t = \pm \frac{1}{2}$  for neutron and proton respectively, and the other quantum number  $i$ . The Dirac spinor has the form:

$$\psi(\vec{r}) = \begin{pmatrix} i \frac{G_i^{lj}(r)}{r} Y_{jm}^l(\theta, \phi) \\ \frac{F_i^{lj}(r)}{r} (\vec{\sigma} \cdot \hat{r}) Y_{jm}^l(\theta, \phi) \end{pmatrix} \chi_t(t), \quad (8)$$

where  $Y_{jm}^l(\theta, \phi)$  are the spinor spherical harmonics and  $G_i^{lj}(r)$  and  $F_i^{lj}(r)$  are the remaining radial wave function for upper and lower components. They are normalized according to

$$\int_0^\infty dr (|G_i^{lj}(r)|^2 + |F_i^{lj}(r)|^2) = 1. \quad (9)$$

The radial equation of spinor Eq. (4) can be reduced as :

$$\begin{cases} \epsilon_i G_i^{lj}(r) = \left( -\frac{\partial}{\partial r} + \frac{\kappa_i}{r} \right) F_i^{lj}(r) + (M + V_S(r) + V_V(r)) G_i^{lj}(r) \\ \epsilon_i F_i^{lj}(r) = \left( +\frac{\partial}{\partial r} + \frac{\kappa_i}{r} \right) G_i^{lj}(r) - (M + V_S(r) - V_V(r)) F_i^{lj}(r). \end{cases} \quad (10)$$

where

$$\kappa = \begin{cases} -(j + 1/2) & \text{for } j = l + 1/2 \\ +(j + 1/2) & \text{for } j = l - 1/2. \end{cases}$$

The meson field equations become simply radical Laplace equations of the form:

$$\left( \frac{\partial^2}{\partial r^2} - \frac{2}{r} \frac{\partial}{\partial r} + m_\phi^2 \right) \phi = s_\phi(r), \quad (11)$$

$m_\phi$  are the meson masses for  $\phi = \sigma, \omega, \rho$  and for photon ( $m_\phi = 0$ ). The source terms are:

$$s_\phi(r) = \begin{cases} -g_\sigma \rho_s - g_2 \sigma^2(r) - g_3 \sigma^3(r) & \text{for the } \sigma \text{ field} \\ g_\omega \rho_v & \text{for the } \omega \text{ field} \\ g_\rho \rho_3(r) & \text{for the } \rho \text{ field} \\ e \rho_c(r) & \text{for the Coulomb field,} \end{cases} \quad (12)$$

$$\begin{cases} 4\pi r^2 \rho_s(r) = \sum_{i=1}^A (|G_i(r)|^2 - |F_i(r)|^2) \\ 4\pi r^2 \rho_v(r) = \sum_{i=1}^A (|G_i(r)|^2 + |F_i(r)|^2) \\ 4\pi r^2 \rho_3(r) = \sum_{p=1}^Z (|G_p(r)|^2 + |F_p(r)|^2) - \sum_{n=1}^N (|G_n(r)|^2 + |F_n(r)|^2) \\ 4\pi r^2 \rho_c(r) = \sum_{p=1}^Z (|G_p(r)|^2 + |F_p(r)|^2). \end{cases} \quad (13)$$

The Laplace equation can in principle be solved by the Green function:

$$\phi(r) = \int_0^\infty r'^2 dr' G_\phi(r, r') s_\phi(r'), \quad (14)$$

where for massive fields

$$G_\phi(r, r') = \frac{1}{2m_\phi} \frac{1}{rr'} (e^{-m_\phi|r-r'|} - e^{-m_\phi|r+r'|}) \quad (15)$$

and for Coulomb field

$$G_\phi(r, r') = \begin{cases} 1/r & \text{for } r > r' \\ 1/r' & \text{for } r < r'. \end{cases} \quad (16)$$

The Eqs.(10) and (11) could be solved self-consistently in the usual RMF approximation.

For RMF, however, as the classical meson fields are used, the equations of motion for nucleons

derived from Eq.(1) do not contain pairing interaction. In order to have pairing interaction, one has to quantize the meson fields which leads to a Hamiltonian with two-body interaction. Following the standard procedure of Bogoliubov transformation, a Dirac Hartree-Bogoliubov equation could be derived and then a unified description of the mean field and pairing correlation in nuclei could be achieved. For the details, see Ref.<sup>4</sup> and the references therein. The RHB equations are as following:

$$\int d^3r' \begin{pmatrix} h - \lambda & \Delta \\ \Delta & -h + \lambda \end{pmatrix} \begin{pmatrix} \psi_U \\ \psi_V \end{pmatrix} = E \begin{pmatrix} \psi_U \\ \psi_V \end{pmatrix}, \quad (17)$$

where

$$h(\vec{r}, \vec{r}') = [\vec{\alpha} \cdot \vec{p} + V_V(\vec{r}) + \beta(M + V_S(\vec{r}))] \delta(\vec{r}, \vec{r}') \quad (18)$$

is the Dirac Hamiltonian and the Fock term has been neglected as is usually done in RMF. The pairing potential is :

$$\Delta_{kk'}(\vec{r}, \vec{r}') = \int d^3r_1 \int d^3r'_1 \sum_{\tilde{k}\tilde{k}'} V_{kk',\tilde{k}\tilde{k}'}(\vec{r}\vec{r}'; \vec{r}_1\vec{r}'_1) \kappa_{\tilde{k}\tilde{k}'}(\vec{r}_1, \vec{r}'_1). \quad (19)$$

It is obtained from one-meson exchange interaction  $V_{kk',\tilde{k}\tilde{k}'}(\vec{r}\vec{r}'; \vec{r}_1\vec{r}'_1)$  in the  $pp$ -channel and the pairing tensor  $\kappa = V^* U^T$

$$\kappa_{kk'}(\vec{r}, \vec{r}') = <|a_k a_{k'}|> = \psi_V^k(\vec{r})^* \psi_U^{k'}(\vec{r}') \quad (20)$$

The nuclear density is as following:

$$\rho(\vec{r}, \vec{r}') = \sum_i^{lj} \psi_V^{ilj}(\vec{r})^* \psi_V^{ilj}(\vec{r}'). \quad (21)$$

As in Ref.<sup>4</sup>,  $V_{kk',\tilde{k}\tilde{k}'}$  used for the pairing potential in Eq.(19) is either the density-dependent two-body force of zero range with the interaction strength  $V_0$  and the nuclear matter density  $\rho_0$ :

$$V(\mathbf{r}_1, \mathbf{r}_2) = V_0 \delta(\mathbf{r}_1 - \mathbf{r}_2) \frac{1}{4} [1 - \boldsymbol{\sigma}_1 \boldsymbol{\sigma}_2] \left(1 - \frac{\rho(r)}{\rho_0}\right) \quad (22)$$

or Gogny-type finite range force with the parameter  $\mu_i$ ,  $W_i$ ,  $B_i$ ,  $H_i$  and  $M_i$  ( $i = 1, 2$ ) as the finite range part of the Gogny force<sup>11</sup>:

$$V(\mathbf{r}_1, \mathbf{r}_2) = \sum_{i=1,2} e^{((\mathbf{r}_1 - \mathbf{r}_2)/\mu_i)^2} (W_i + B_i P^\sigma - H_i P^\tau - M_i P^\sigma P^\tau) \quad (23)$$

A Lagrange multiplier  $\lambda$  is introduced to fix the particle number for the neutron and proton as  $N = \text{Tr}\rho_n$  and  $Z = \text{Tr}\rho_p$ .

In order to describe both the continuum and the bound states self-consistently, the RHB theory must be solved in coordinate representation, i.e., the Relativistic Continuum Hartree-Bogoliubov ( RCHB ) theory<sup>4</sup>. It is then applicable to both exotic nuclei and normal nuclei. In Eq. (17), the spectrum of the system is unbound from above and from below the Fermi surface, and the eigenstates occur in pairs of opposite energies. When spherical symmetry is imposed on the solution of the RCHB equations, the wave function can be conveniently written as

$$\psi_U^i = \begin{pmatrix} i \frac{G_U^{ilj}(r)}{r} \\ \frac{F_U^{ilj}(r)}{r} (\vec{\sigma} \cdot \hat{\vec{r}}) \end{pmatrix} Y_{jm}^l(\theta, \phi) \chi_t(t), \quad \psi_V^i = \begin{pmatrix} i \frac{G_V^{ilj}(r)}{r} \\ \frac{F_V^{ilj}(r)}{r} (\vec{\sigma} \cdot \hat{\vec{r}}) \end{pmatrix} Y_{jm}^l(\theta, \phi) \chi_t(t). \quad (24)$$

The above equation Eq.(17) depends only on the radial coordinates and can be expressed as the following integro-differential equation:

$$\begin{cases} \frac{dG_U(r)}{dr} + \frac{\kappa}{r} G_U(r) - (E + \lambda - V_V(r) + V_S(r)) F_U(r) + r \int r' dr' \Delta(r, r') F_V(r') = 0 \\ \frac{dF_U(r)}{dr} - \frac{\kappa}{r} F_U(r) + (E + \lambda - V_V(r) - V_S(r)) G_U(r) + r \int r' dr' \Delta(r, r') G_V(r') = 0 \\ \frac{dG_V(r)}{dr} + \frac{\kappa}{r} G_V(r) + (E - \lambda + V_V(r) - V_S(r)) F_V(r) + r \int r' dr' \Delta(r, r') F_U(r') = 0 \\ \frac{dF_V(r)}{dr} - \frac{\kappa}{r} F_V(r) - (E - \lambda + V_V(r) + V_S(r)) G_V(r) + r \int r' dr' \Delta(r, r') G_U(r') = 0, \end{cases} \quad (25)$$

where the nucleon mass is included in the scalar potential  $V_S(r)$ . Eq.(25), in the case of  $\delta$ -force Eq.(22), is reduced to normal coupled differential equations and can be solved with shooting method by Runge-Kutta algorithms. For the case of Gogny force, the coupled integro-differential equations are discretized in the space and solved by the finite element methods, see Ref.<sup>4</sup> Instead of solving Eqs.(10) and (11) self-consistently for the RMF case,

now we have to solve Eqs.(25) and (11) self-consistently for the RCHB case. As the calculation for Gogny force is very time-consuming, we use them for one nucleus and fixed the interaction strength in  $\delta$ -force Eq.(22).

### 3. Results and discussion

The procedure to solve the RCHB equations is the same as in Ref.<sup>4</sup>, we solve the RCHB equations in a box of the size  $R = 25$  fm and a step size of 0.1 fm for the parameter set NLSH<sup>12</sup> self-consistently. The  $\delta$ -force is used in the pairing channel and its strength is properly fixed by the Gogny force as in Ref.<sup>4</sup>. The number of continuum taken into account is decided by a cutoff energy, i.e., only the levels lying within 120 MeV from the Fermi level are taken into account. For  $\rho_0$  we use the nuclear matter density  $0.152$  fm<sup>-3</sup>. The strength  $V_0$  of Eq.(22) is determined by adjusting the corresponding pairing energy  $-\frac{1}{2}\text{Tr}\Delta\kappa$  to that of the Gogny force D1S<sup>11</sup> in <sup>150</sup>Sn.

In Fig. 1, we show the two neutron separation energies  $S_{2n}$  of even tin isotopes as a function of the neutron number  $N$  from the proton drip-line to the neutron drip-line, including the experimental data ( solid points ), and RCHB with  $\delta$ -force ( open circles ). The RCHB calculation reproduces the experimental data quite well. They show a strong kink at  $N = 50$  and  $N = 82$ . The drip line nucleus is predicted at <sup>176</sup>Sn in the present calculation. The available empirical data of  $S_{2n}$  have been well reproduced.

The magnitude of the kink at  $N = 82$  shows that the shell effects in the RMF theory are observed to be strong at  $N = 82$ . Measurement of the mass of <sup>134</sup>Sn, in future, would clarify the nature of the shell effects at  $N = 82$ . Apart from the kinks observed at  $N = 50$  and  $N = 82$ ,  $S_{2n}$  gradually decrease with  $N$ . The  $S_{2n}$  near drip line nuclei <sup>176</sup>Sn decreases relatively faster than the case in light nuclei, e.g., Na isotopes<sup>9</sup>. This is due to the effects of centrifugal barrier. In Sn isotopes, the orbital  $1i_{13/2}$  is just above the threshold for nuclei near the drip line. Due to its big centrifugal barrier, particles filled in  $1i_{13/2}$  do not contribute to the binding, although the potential become highly diffuse. In light nuclei like Na isotopes,

the orbital  $2p_{1/2}$  and  $2p_{3/2}$  are just above the threshold. They gain binding energy due to the diffuseness of potential with  $N$ . Therefore the total binding energies of the Na isotopes remain unchanged with  $N$  near the drip line.

The neutron, proton, matter, and charge radii for all even Sn isotopes are given in Table 1. The neutron and matter radii increase with the neutron number. Also the proton radii increases slowly after  $^{100}\text{Sn}$ .

Encouraged by the success in describing the  $S_{2n}$  for tin isotopes, we proceed to examine the spin-orbital splitting for the whole isotopes. As an example, spin-orbital splitting

$$E_{ls} = \frac{E_{lj=l-1/2} - E_{lj=l+1/2}}{2l + 1} \quad (26)$$

versus the binding energy:

$$E = \frac{(l + 1)E_{lj=l-1/2} + lE_{lj=l+1/2}}{2l + 1} \quad (27)$$

in  $^{110}\text{Sn}$ ,  $^{120}\text{Sn}$ ,  $^{130}\text{Sn}$ ,  $^{140}\text{Sn}$ ,  $^{150}\text{Sn}$ ,  $^{160}\text{Sn}$ , and  $^{170}\text{Sn}$  are given in Fig. 2 for the neutron spin-orbital partners  $(1d_{3/2}, 1d_{5/2})$ ,  $(1g_{7/2}, 1g_{9/2})$ ,  $(1i_{11/2}, 1i_{13/2})$ ,  $(1p_{1/2}, 1p_{3/2})$ ,  $(1f_{5/2}, 1f_{7/2})$ , and  $(1h_{9/2}, 1h_{11/2})$ , and the proton spin-orbital partners  $(1d_{3/2}, 1d_{5/2})$ , and  $(1f_{5/2}, 1f_{7/2})$ . It is very interesting to see that the spin-orbital splitting for the neutron and proton is very close to each other, at least for  $(1d_{3/2}, 1d_{5/2})$ , and  $(1f_{5/2}, 1f_{7/2})$  cases. The splitting decreases monotonically from the proton drip line to the neutron drip line for all the partners. To see the underlying reason of this behavior, it is very helpful to examine the origin of the spin-orbital splitting in the Dirac equation. For the Dirac nucleon moving in a scalar and vector potentials, its equation of motion could be de-coupled and reduced for the upper component and the lower component, respectively. If it is reduced in the lower component, it will be related with another interesting topic – the pseudo-spin symmetry discussed in Ref.<sup>13</sup> and the references therein. For the moment, we are interested in the spin-orbital splitting, the Dirac equation can be reduced for the upper component as following:

$$[\frac{d^2}{dr^2} - \frac{1}{E + 2M - V_V + V_S} \frac{d(2M - V_V + V_S)}{dr} \frac{d}{dr}]G_i^{lj}(r)$$

$$\begin{aligned}
& - \left[ \frac{\kappa(1+\kappa)}{r^2} - \frac{1}{E+2M-V_V+V_S} \frac{\kappa}{r} \frac{d(2M-V_V+V_S)}{dr} \right] G_i^{lj}(r) \\
& = - (E+2M-V_V+V_S)(E-V_V-V_S) G_i^{lj}(r)
\end{aligned} \tag{28}$$

where

$$\kappa = \begin{cases} -l-1, & j = l+1/2 \\ l, & j = l-1/2 \end{cases} \tag{29}$$

The spin-orbital splitting is due to the corresponding spin-orbital potential

$$\frac{1}{E+2M-V_V+V_S} \frac{\kappa}{r} \frac{d(2M-V_V+V_S)}{dr} \tag{30}$$

with some proper normalization factor. It is seen that the spin-orbital splitting in RMF is energy dependent and they depends on the derivative of the potential  $2M - V_V + V_S$  as well as the particle distribution. Therefore we introduce the so-called spin-orbital potential:  $V_{ls} = \frac{\kappa}{r} \frac{d(2M - V_V + V_S)}{dr}$ . The  $V_{ls}$  for  $^{110}\text{Sn}$ ,  $^{140}\text{Sn}$ , and  $^{170}\text{Sn}$ , are given in Fig.3. The  $V_{ls}$  for both proton and neutron are almost the same, as the potential  $V_V - V_S$  is a big quantity ( $\sim 700$  MeV), the isospin dependence in the spin-orbital potential could be neglected. Therefore the proton and neutron  $V_{ls}$  are the same in the present model. That is the reason why the spin-orbital splitting for the neutron and proton is very close to each other in Fig. 2. From  $^{110}\text{Sn}$  to  $^{170}\text{Sn}$ , the amplitude of  $V_{ls}$  decreases monotonically due to the surface diffuseness.

For the decline of the spin-orbital splitting, it come from the diffuseness of the potential or the outwards tendency of the potential. The diffuseness of the neutron potentials  $V_V + V_S$  are given in Fig. 4 for  $^{110}\text{Sn}$ ,  $^{120}\text{Sn}$ ,  $^{130}\text{Sn}$ ,  $^{140}\text{Sn}$ ,  $^{150}\text{Sn}$ ,  $^{160}\text{Sn}$ , and  $^{170}\text{Sn}$ . It is seen that the depth of the potential decreases monotonically from the proton drip line to the neutron drip line and the surface of the potential moves outwards. The inserted figures gives the radii  $R_0$  at which  $V_V + V_S = -10$  MeV as a function of the mass number. The proton potentials  $V_V + V_S$  for  $^{110}\text{Sn}$ ,  $^{120}\text{Sn}$ ,  $^{130}\text{Sn}$ ,  $^{140}\text{Sn}$ ,  $^{150}\text{Sn}$ ,  $^{160}\text{Sn}$ , and  $^{170}\text{Sn}$  are given in Fig. 5. With the increase of the neutron number, the proton potentials are pushed towards outside as well due to the proton-neutron interaction.

Similar neutron potentials  $V_V - V_S$  for  $^{100}\text{Sn}$ ,  $^{110}\text{Sn}$ ,  $^{120}\text{Sn}$ ,  $^{130}\text{Sn}$ ,  $^{140}\text{Sn}$ ,  $^{150}\text{Sn}$ ,  $^{160}\text{Sn}$ , and  $^{170}\text{Sn}$  are given in Fig.6 and its inserted figures gives the radii  $R_0$  at which  $V_V - V_S = 100$  MeV as a function of the mass number. As seen in the above equations, the spin-orbital splitting is related with the derivative of the potential  $V_V - V_S$ . The surface diffuseness happens for both the vector and scalar potential, it occurs in  $V_V - V_S$  and  $V_V + V_S$ .

So far we have started the isospin dependence and showed how the spin-orbital splitting is reduced due to the diffuseness of the potential. Another feature of the spin-orbital splitting is the energy-dependence given in Eq.(28). The single particle levels in the canonical basis for the neutron in  $^{170}\text{Sn}$  are given in Fig.7. The neutron potentials  $V_V + V_S$  is represented by the solid line and the Fermi level is represented by a dashed-line. The depth of the neutron potential in  $^{170}\text{Sn}$  is about -60 MeV and the single particle levels begins from -55 MeV for  $1s_{1/2}$ . The spin-orbital partners appear in the order of the energy  $(1p_{3/2}, 1p_{1/2})$ ,  $(1d_{5/2}, 1d_{3/2})$ ,  $(1f_{7/2}, 1f_{5/2})$ ,  $(2p_{3/2}, 2p_{1/2})$ ,  $(1g_{9/2}, 1g_{7/2})$ ,  $(2d_{5/2}, 2d_{3/2})$ ,  $(1h_{11/2}, 1h_{9/2})$ ,  $(2f_{7/2}, 2f_{5/2})$ ,  $(3p_{3/2}, 3p_{1/2})$ , and  $(1i_{13/2}, 1i_{11/2})$ , etc. The larger spin-orbital splitting for the same  $l$  occurs when the particle is located in the middle of the potential. As it can be seen, the spin-orbital splitting in  $(2p_{3/2}, 2p_{1/2})$  partners is twice as large as that in  $(1p_{3/2}, 1p_{1/2})$  and thrice as large as that in  $(3p_{3/2}, 3p_{1/2})$ . Their energy dependence is clearly seen. In Fig. 8, the spin-orbit splitting in Eq.(26) versus the binding energy in Eq.(27): in  $^{170}\text{Sn}$  are also given in Fig.7 for  $(p_{3/2}, p_{1/2})$ ,  $(d_{5/2}, d_{3/2})$ ,  $(f_{7/2}, f_{5/2})$ ,  $(g_{9/2}, g_{7/2})$ ,  $(h_{9/2}, h_{11/2})$ , and  $(i_{11/2}, i_{13/2})$  partners. It gives a strong energy dependence of the spin-orbital splitting. Similar pattern is also appeared in other tin isotopes, but here we just choose  $^{170}\text{Sn}$  as an example.

As mentioned above, the spin-orbital splitting is mainly due to the corresponding spin-orbital potential Eq.(30), which decreases with the diffuseness of the potential. However, for the single particle levels in the same nuclei, the spin-orbital potential is the same, the difference is due to the particle distribution relative to the spin-orbital potential. In Fig. 9, the spin-orbital potential  $V_{ls}$  multiplied by the density distributions for  $p_{1/2}$  orbital in  $^{170}\text{Sn}$

is given in the upper panel, and the spin-orbital potential and the probability distribution of the  $p$ -wave in  $^{170}\text{Sn}$  is given in the lower panel. As seen in the lower panel, the particle distributions move outside with the increasing energy. The maximum overlap happens for  $(2p_{3/2}, 2p_{1/2})$ . This clearly explain the features observed in Fig. 8. Another aspect in Fig.8 is that the splitting for  $n = 1$  always increases with  $l$ . This is because the centrifugal barrier keeps the particle away from center and prevent it from running away so that a big overlap always happens for larger  $l$ .

Recent developments in accelerator technology and detection techniques around the world have made it possible to produce and study the nuclei far from the stability line – so called "EXOTIC NUCLEI". Experiments of this kind have brought about a new perspective to nuclear structure physics: e.g., the neutron halo and neutron skin as manifested in the rapid increase in the measured interaction cross-sections in the neutron-rich light nuclei<sup>14,15</sup>. These extremely neutron-rich nuclei and physics connected with the low density matter in the tails of the neutron and proton distributions have attracted a lot of attention in nuclear physics as well as in other fields such as astrophysics. It is therefore of great importance to look into the matter distribution and see how the densities change with the proton to neutron ratio in these nuclei. As the density here is obtained from a fully microscopic and parameter free model, it is well supported by the experimental binding energies. We now proceed to examine the density distributions of the whole chain of tin isotopes and study the relation between the development of halo and shell effects within the model. The density distributions for  $^{100}\text{Sn}$ ,  $^{110}\text{Sn}$ ,  $^{120}\text{Sn}$ ,  $^{130}\text{Sn}$ ,  $^{140}\text{Sn}$ ,  $^{150}\text{Sn}$ ,  $^{160}\text{Sn}$ , and  $^{170}\text{Sn}$  are given for neutron, proton, and matter density in Figs. 10a, 10b, and 10c, respectively. With the increase of  $N$ , the density extends toward outside, only a small increase is observed in the center. For the proton densities in Fig.10b, the density for  $r \leq 4$  fm decreases dramatically, and in reward for this a strong increase in the surface is observed with the increasing of the neutron number, because the proton number is fixed. This is quite different from the case of Na isotopes, where the proton distribution doesn't vary so much with  $N$  in the surface

area<sup>9</sup>. The matter densities for Sn isotopes are given in Fig.10c. Although neutron density increases in the center, it is slower than the decrease in proton. Therefore the total matter density decreases in the center. Due to the proton and neutron interaction, both proton and neutron densities increase in the surface.

Fig. 11 is the same as Fig. 10, but in logarithm scale in order to see the detailed information in the tail. With the increase of  $N$ , the neutron density extends towards outside. The increase of the neutron density beyond  $r = 6$  fm shows a gradual variation, except after  $^{160}\text{Sn}$  where the tail of the neutron density does not change. The isotopes  $^{160-170}\text{Sn}$  have almost the same tail in the density. For the proton, the tail of the proton density in  $^{100}\text{Sn}$  and  $^{110}\text{Sn}$  shows difference from the isotopes with  $N > 60$ , which clearly shows that the tail is a asymptotic behavior mainly determined by the last filled few particles. For the tail of the matter distribution in neutron-rich nuclei, they are mainly determined by the neutron density.

#### 4. Conclusions

The Relativistic Continuum Hartree Bogoliubov ( RCHB ) theory, which is the extension of the Relativistic Mean Field and the Bogoliubov transformation in the coordinate representation, has been used to study the tin isotopes. The pairing correlation is taken into account by a density-dependent force of zero range. RCHB is used to describe the even-even tin isotopes all the way from the proton drip line to the neutron drip line. The theoretical  $S_{2n}$  as well as the neutron, proton, and matter *rms* radii are presented and compared with the experimental values where they exist. The change of the potential surface with the neutron number has been investigated. The diffuseness of the potentials in tin isotopes is analyzed through the spin-orbital splitting in order to provide new way to understand the halo phenomena in exotic nuclei. Summarizing the present investigation We can conclude:

1. The spin-orbital splitting decreases monotonically from the proton drip line to the neutron drip line for all  $l$  partners. The spin-orbital splitting for the neutron and

proton is very close to each other in RCHB, as the potential  $V_V - V_S$  is a big quantity (  $\sim 700$  MeV ) and its isospin dependence in the spin-orbital potential could be neglected. Therefore the proton and neutron  $V_{ls}$  are the same in the present model.

2. For the decreasing of the spin-orbital splitting with  $N$ , it come from the diffuseness of the potential or the outwards push of the potential. The depth of the potential decreases monotonically from the proton drip line to the neutron drip line and the surface of the potential moves outwards. With the neutron number  $N$ , the proton potentials are pushed towards outside as well due to the proton-neutron interaction.
3. A strong energy dependence of the spin-orbital splitting appears in tin isotopes. It is due to the change of wave function. The maximum overlap between the particle distributions and the spin-orbital potential happens when the single particle energy is in the middle of the potential. This energy dependent behavior is stronger for lower  $l$  orbits than the higher  $l$  orbits, as the centrifugal barrier in higher  $l$  orbits keeps the particle away from center and prevent it from running away so that there is always a reasonable overlap with spin-orbital potential.
4. With increase of  $N$ , the neutron density extends towards outside. The increasing of the neutron density beyond  $r = 6$  fm shows a gradual variation with  $N$ . The neutron tail reaches saturation after  $^{160}\text{Sn}$ . For the proton, the tail of the proton density in  $^{100}\text{Sn}$  and  $^{110}\text{Sn}$  shows difference from the isotopes with  $N > 60$ , which clearly shows that the tail is a asymptotic behavior mainly due to the last filled few particles. For the tail of the matter distribution in neutron-rich nuclei, they are mainly determined by the neutron density.
5. With the increase of  $N$ , the density extends toward outside, only a small increase is observed in the center. For the proton, the density for  $r \leq 4$  fm decreases dramatically, and in return for this a strong increase in the surface is observed with the increasing of the neutron number, because the proton number is fixed. Therefore, a slight decrease

in the center of the total matter density is observed.

## REFERENCES

1. I. Tanihata et al, Phys. Rev. Lett. **55** (1985) 2676
2. J. Meng, and P. Ring, Phys. Rev. Lett. **77** (1996) 3963.
3. J. Meng, and P. Ring, Phys. Rev. Lett. **80** (1998) 460.
4. J. Meng, Nucl. Phys. **A635** (1998) 3.
5. M. Zhukov et al, Phys. Rep. **231** (1993) 151
6. J.Dobaczewski, H.Flocard and J.Treiner, Nucl.Phys. **A422** (1984) 103.
7. J. Terasaki, et al , Nucl. Phys. **A600** (1996) 371
8. T.T.S.Kuo, et al, Phys. Rev. Lett. **78** (1997) 2708
9. J. Meng, I. Tanihata and S. Yamaji, Phys. Lett. **B419** (1998) 1.
10. J. Boguta, A.R. Bodmer, Nucl. Phys. **A292** (1977) 413
11. J.F. Berger et al, Nucl. Phys. **A428** (1984) 32c
12. M.M. Sharma, M.A. Nagarajan, and P. Ring, Phys. Lett. **B312** (1993) 377
13. J. Meng, K.Sugawara-Tanabe, S.Yamaji, P. Ring and A.Arima, Phys. Rev. C58 (1998) R628
14. I.Tanihata, Prog.Part.and Nucl.Phys.,**35** ( 1995 ) 505
15. P.G. Hansen, A.S. Jensen, and B. Jonson, Ann. Rev. Nucl. Part. Sci. **45** (1995) 591

TABLES

Table 1. The neutron, proton, matter, and charge radii for Sn isotopes

A	$r_n$	$r_p$	$r_m$	$r_c$	A	$r_n$	$r_p$	$r_m$	$r_c$
96	4.254	4.393	4.327	4.465	140	5.154	4.712	5.000	4.779
98	4.288	4.393	4.342	4.465	142	5.199	4.730	5.039	4.797
100	4.320	4.393	4.357	4.465	144	5.243	4.748	5.077	4.815
102	4.373	4.414	4.393	4.486	146	5.287	4.765	5.114	4.831
104	4.422	4.433	4.428	4.505	148	5.331	4.781	5.152	4.847
106	4.469	4.452	4.461	4.523	150	5.375	4.797	5.189	4.863
108	4.515	4.470	4.494	4.541	152	5.419	4.812	5.227	4.878
110	4.556	4.487	4.525	4.558	154	5.463	4.826	5.264	4.892
112	4.601	4.502	4.557	4.573	156	5.506	4.839	5.301	4.905
114	4.643	4.517	4.588	4.588	158	5.549	4.853	5.338	4.918
116	4.684	4.532	4.619	4.602	160	5.590	4.866	5.374	4.931
118	4.721	4.545	4.647	4.615	162	5.628	4.879	5.408	4.944
120	4.760	4.559	4.677	4.629	164	5.661	4.894	5.439	4.959
122	4.797	4.572	4.706	4.642	166	5.690	4.910	5.467	4.974
124	4.833	4.586	4.735	4.655	168	5.715	4.926	5.492	4.991
126	4.868	4.599	4.763	4.668	170	5.739	4.944	5.517	5.008
128	4.902	4.611	4.790	4.680	172	5.761	4.961	5.541	5.025
130	4.934	4.624	4.817	4.692	174	5.783	4.979	5.564	5.043
132	4.964	4.636	4.842	4.704					
134	5.013	4.656	4.883	4.724					
136	5.061	4.675	4.923	4.743					
138	5.108	4.694	4.962	4.761					

## Figure Captions

**Fig. 1** Two-neutron separation energies  $S_{2n}$  of even Sn isotopes as a function of  $N$ , including the experimental data ( solid points ) and the RCHB calculation with  $\delta$ -force ( open circles ).

**Fig. 2** The neutron spin-orbit splitting  $E_{ls} = \frac{E_{lj=l-1/2} - E_{lj=l+1/2}}{2l+1}$  versus the mass number  $A$  in tin isotopes for neutron  $(1d_{3/2}, 1d_{5/2})$ ,  $(1g_{7/2}, 1g_{9/2})$ ,  $(1i_{11/2}, 1i_{13/2})$ ,  $(1p_{1/2}, 1p_{3/2})$ ,  $(1f_{5/2}, 1f_{7/2})$ , and  $(1h_{9/2}, 1h_{11/2})$  orbital and proton  $(1d_{3/2}, 1d_{5/2})$ , and  $(1f_{5/2}, 1f_{7/2})$  orbital, respectively.

**Fig. 3** The derivative of the neutron potentials  $V_V(r) - V_S(r)$  for  $^{110}\text{Sn}$ ,  $^{140}\text{Sn}$ , and  $^{170}\text{Sn}$ .

**Fig. 4** The neutron potentials  $V_V(r) + V_S(r)$  for  $^{100}\text{Sn}$ ,  $^{110}\text{Sn}$ ,  $^{120}\text{Sn}$ ,  $^{130}\text{Sn}$ ,  $^{140}\text{Sn}$ ,  $^{150}\text{Sn}$ ,  $^{160}\text{Sn}$ , and  $^{170}\text{Sn}$ . In order to examine the surface diffuseness more clearly, the radii  $R_0$  at which  $V_V(R_0) + V_S(R_0) = -10$  MeV has been given as an inserted figure.

**Fig. 5** The proton potentials  $V_V(r) + V_S(r)$  for  $^{110}\text{Sn}$ ,  $^{120}\text{Sn}$ ,  $^{130}\text{Sn}$ ,  $^{140}\text{Sn}$ ,  $^{150}\text{Sn}$ ,  $^{160}\text{Sn}$ , and  $^{170}\text{Sn}$ . In order to examine the surface diffuseness more clearly, the radii  $R_0$  at which  $V_V(R_0) + V_S(R_0) = -10$  MeV has been given as an inserted figure.

**Fig. 6** The neutron potentials  $V_V(r) - V_S(r)$  for  $^{100}\text{Sn}$ ,  $^{110}\text{Sn}$ ,  $^{120}\text{Sn}$ ,  $^{130}\text{Sn}$ ,  $^{140}\text{Sn}$ ,  $^{150}\text{Sn}$ ,  $^{160}\text{Sn}$ , and  $^{170}\text{Sn}$ . In order to examine the surface diffuseness more clearly, the radii  $R_0$  at which  $V_V(R_0) - V_S(R_0) = 100$  MeV has been given as an inserted figure.

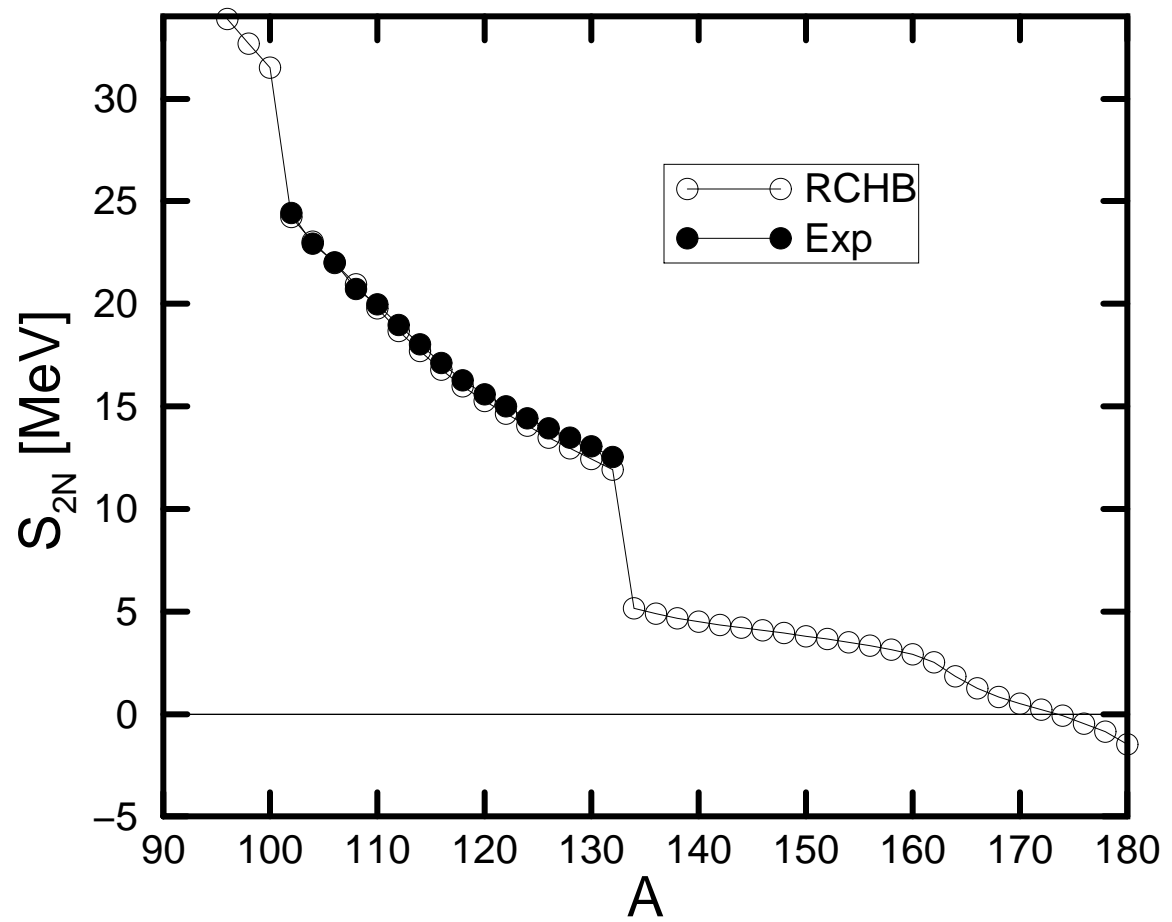
**Fig. 7** The single particle levels in the canonical basis for the neutron in  $^{170}\text{Sn}$ . The neutron potentials  $V_V(r) + V_S(r)$  is represented by the solid line and the Fermi level is represented by a dashed-line.

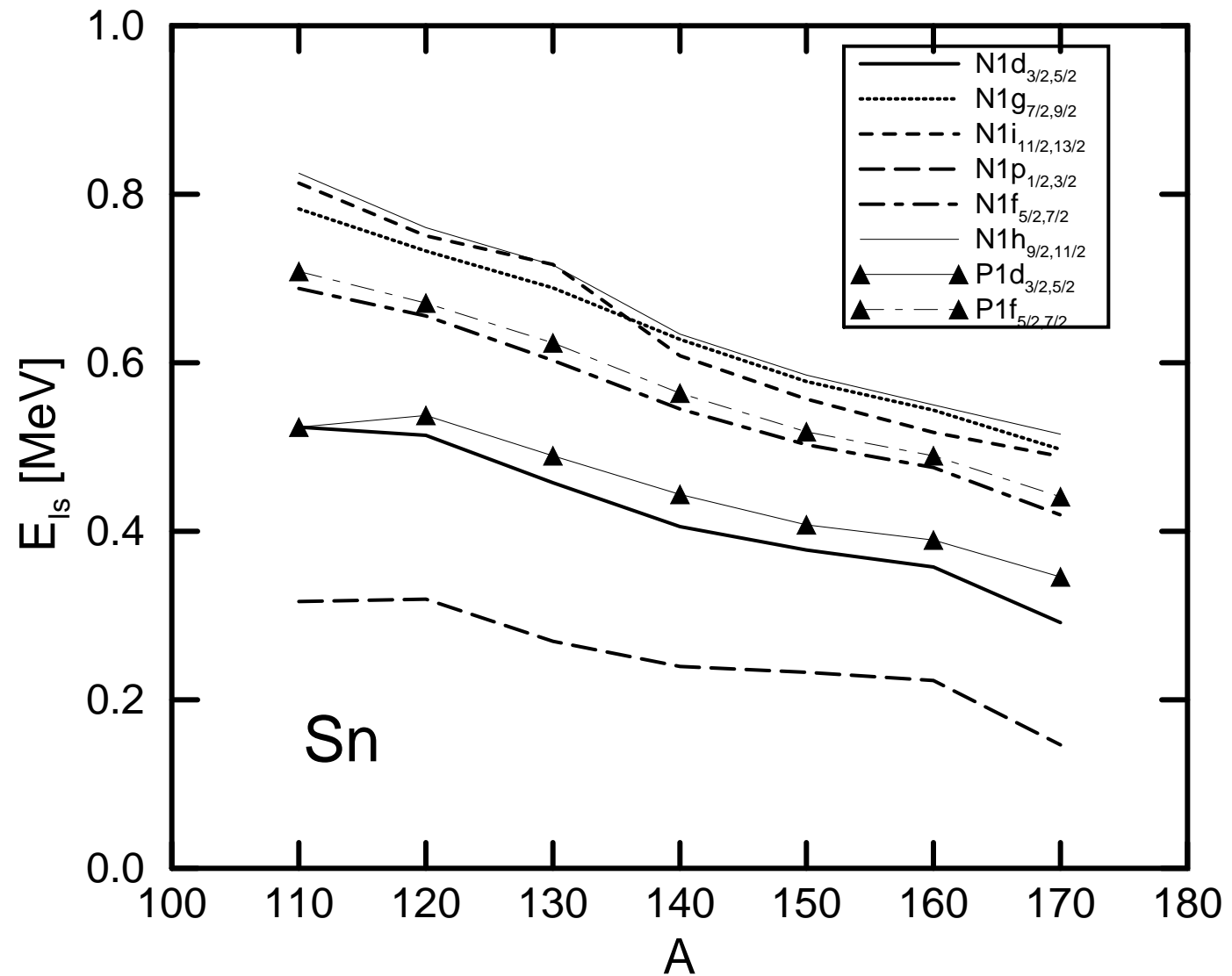
**Fig. 8** The energy dependence of neutron spin-orbital splitting in  $^{170}\text{Sn}$ ,

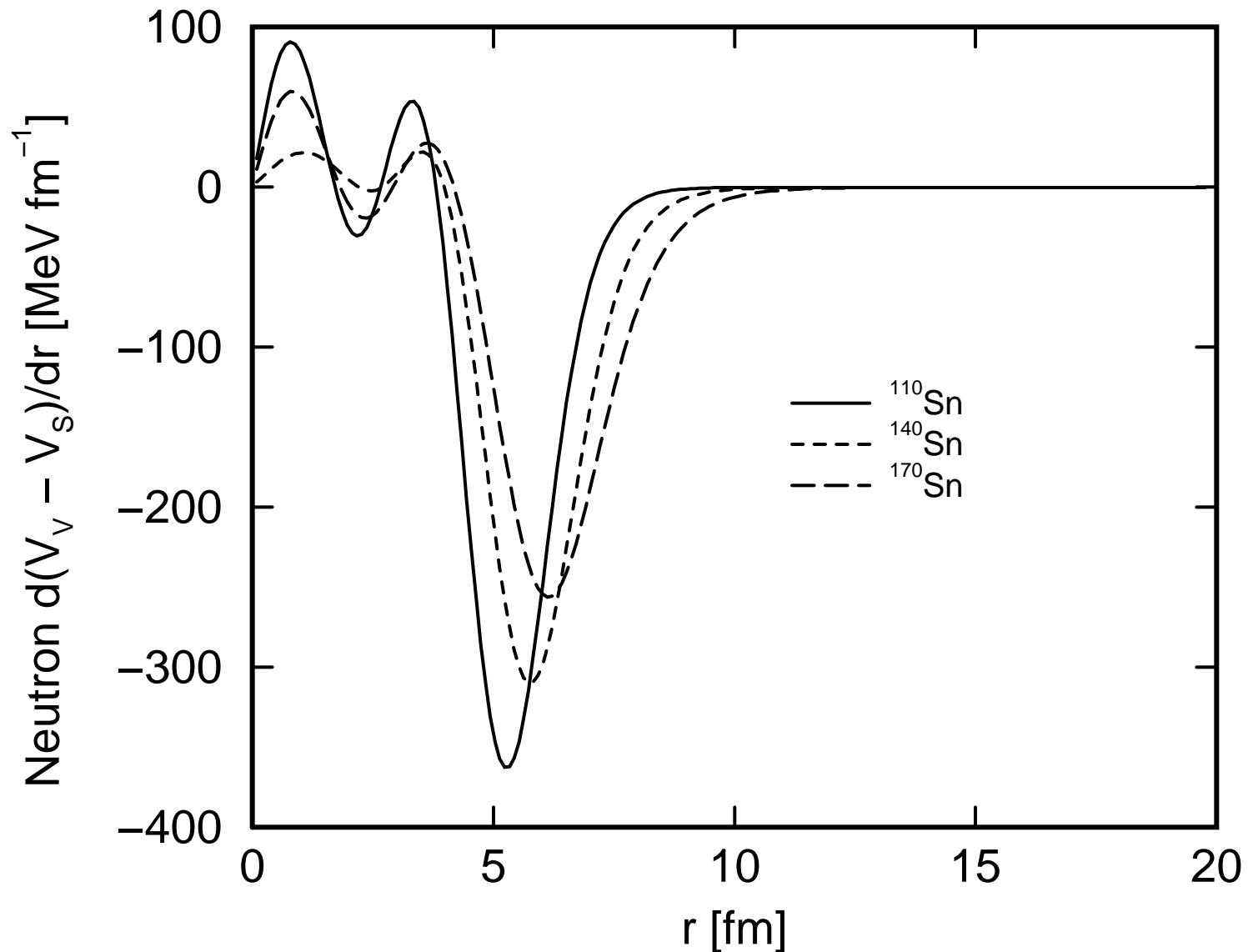
**Fig. 9** The upper panel is the spin-orbital potential  $V_{ls}$  multiplied by the density distributions of the  $p_{1/2}$  orbital. The lower panel is the spin-orbital potential and the density distributions for  $p_{1/2}$  orbital in  $^{170}\text{Sn}$ .

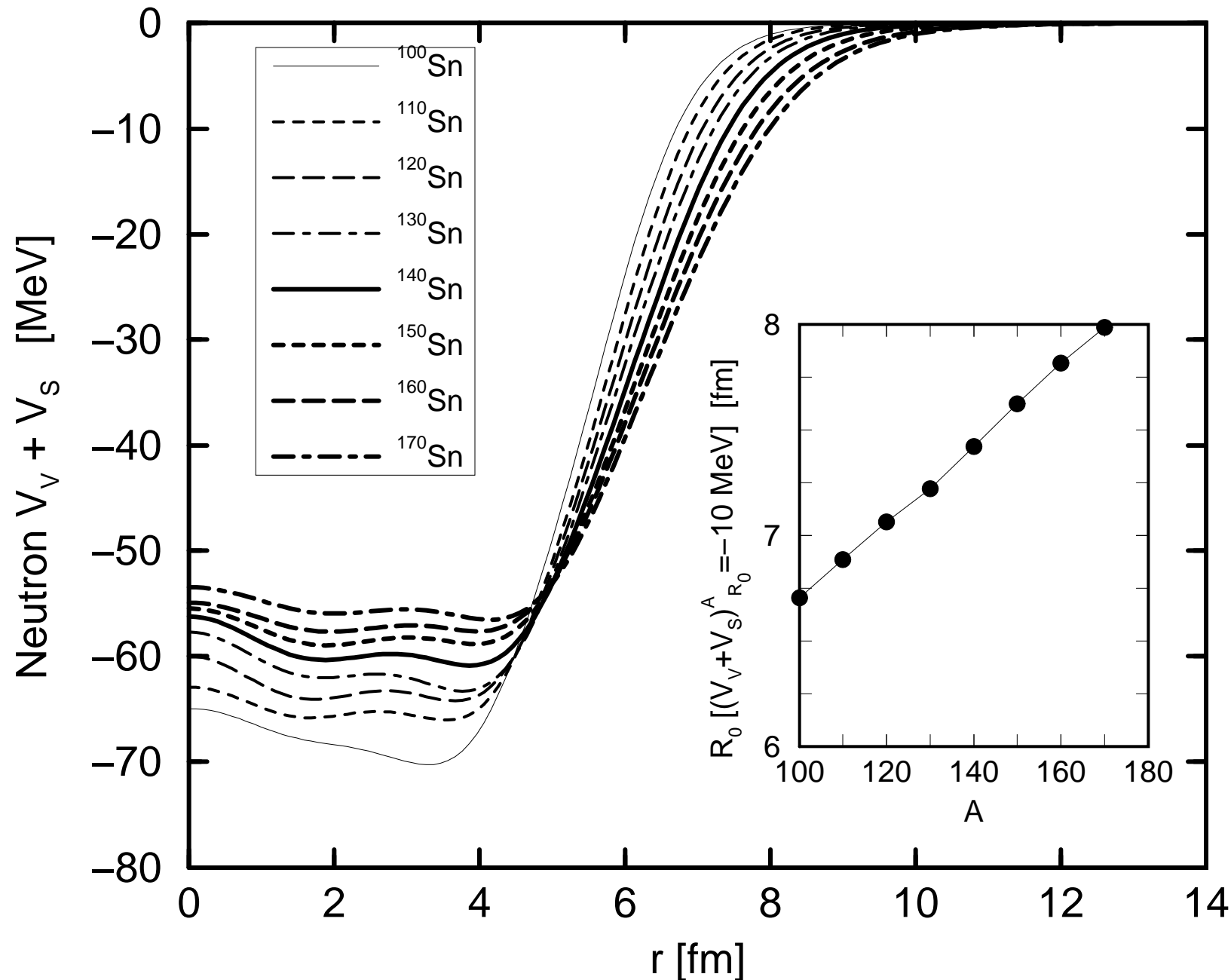
**Fig. 10** The neutron (a) , proton (b), and matter (c) density distributions in Sn isotopes.

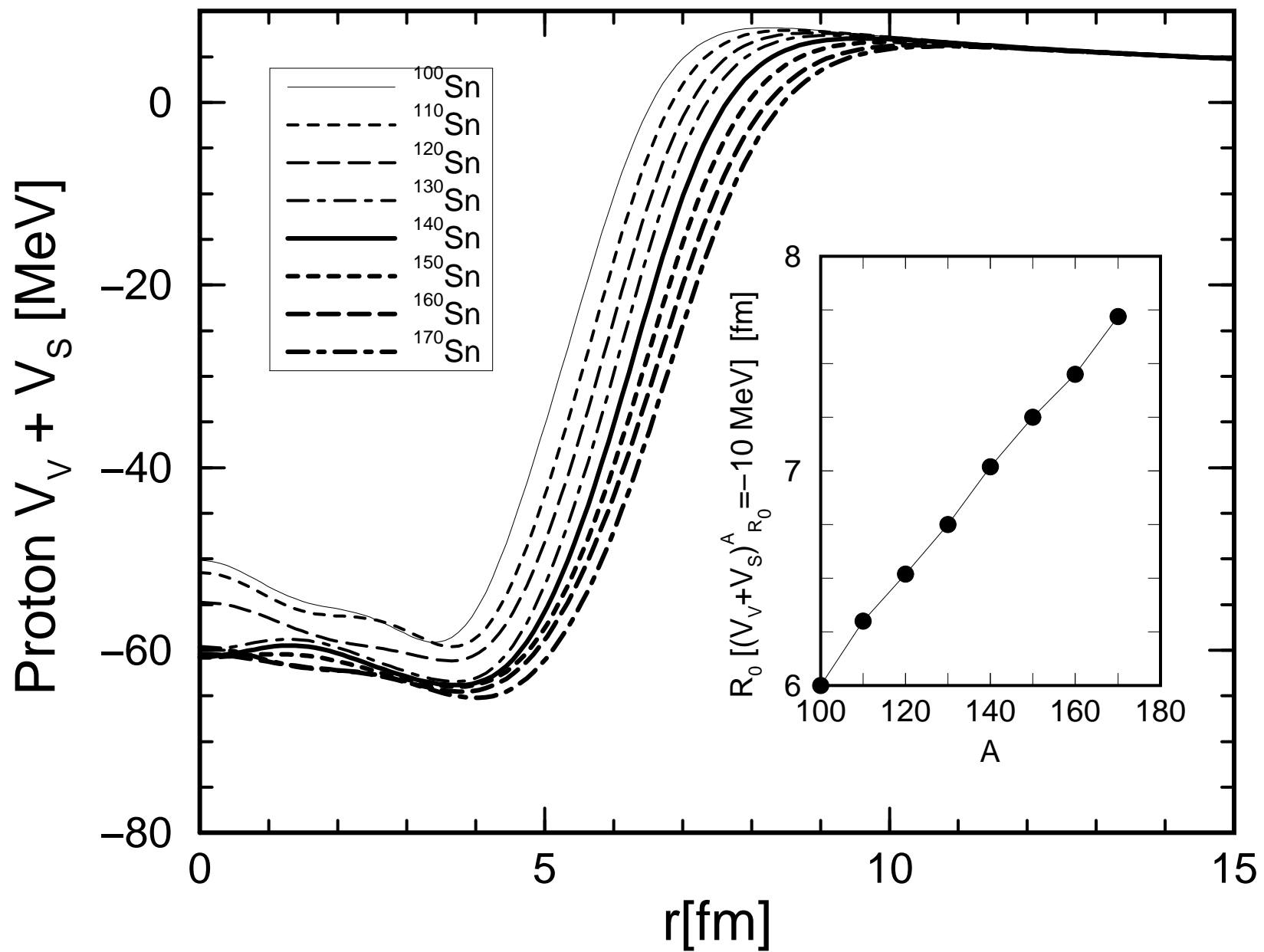
**Fig. 11** The same as Fig. 10, but in logarithm scale.

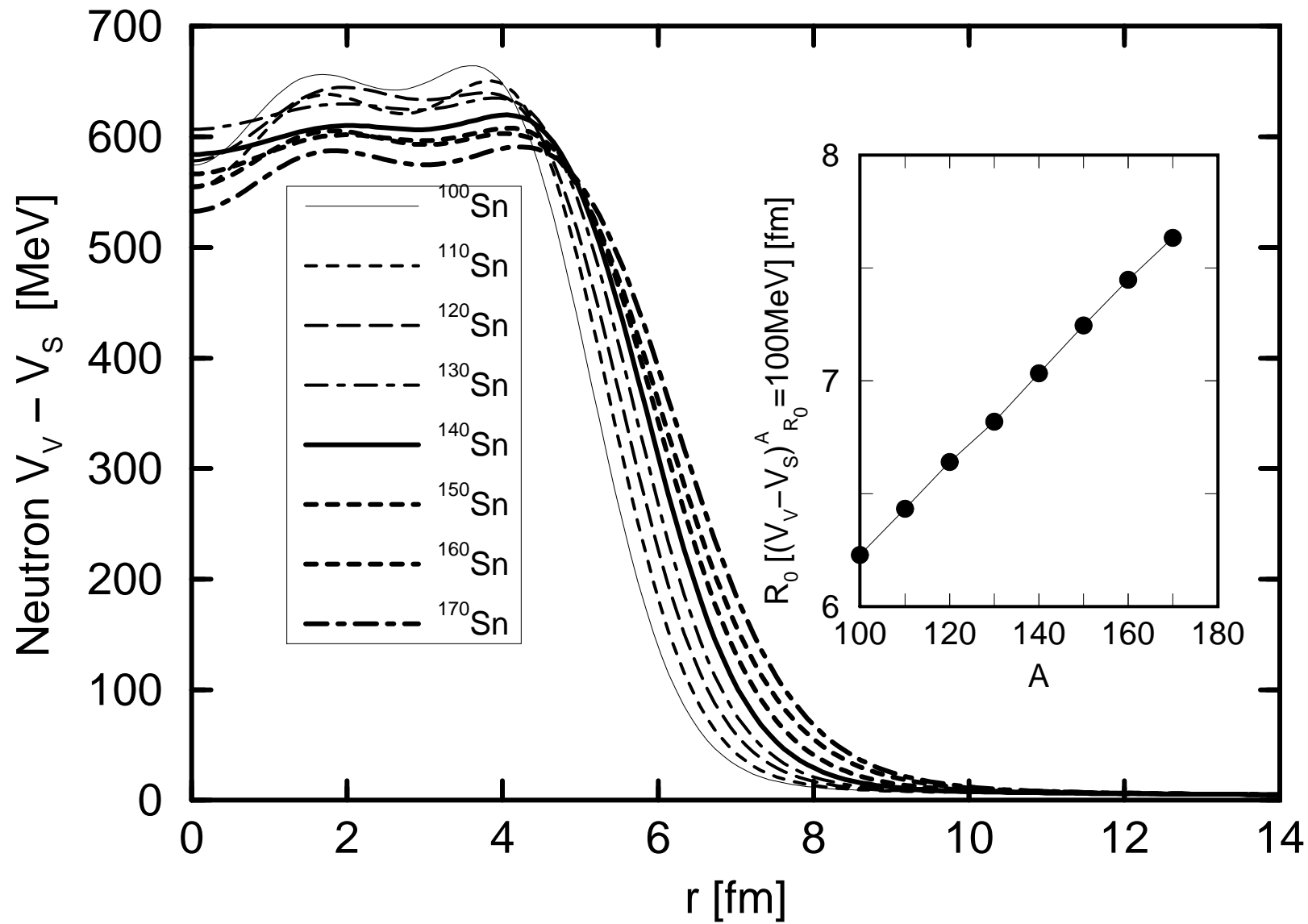


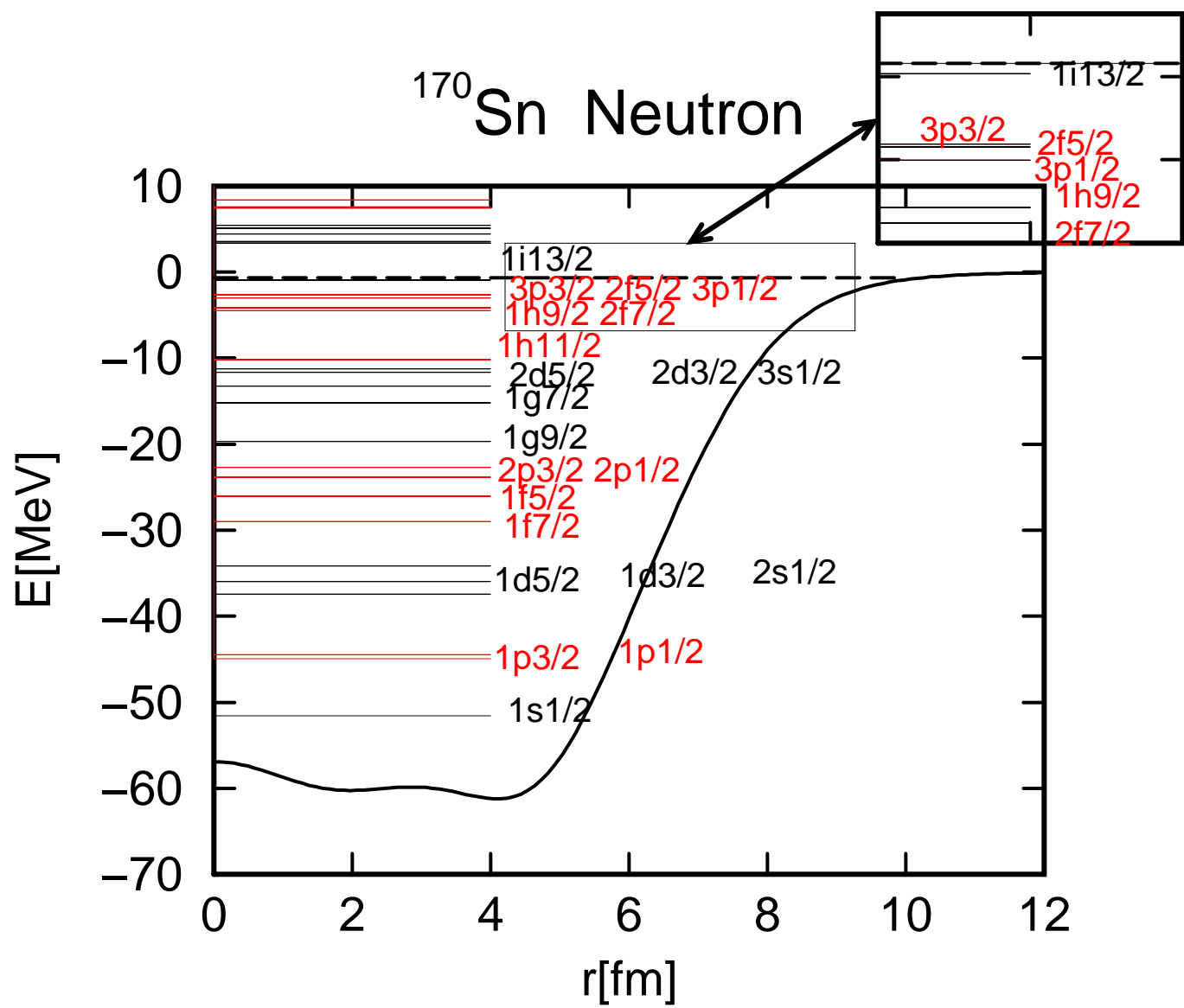












$^{170}\text{Sn}$ 